Journal of the European Ceramic Society 44 (2024) 2571–2580

Contents lists available at ScienceDirect

Journal of the European Ceramic Society

journal homepage: www.elsevier.com/locate/jeurceramsoc

Improving the strength of β-TCP scaffolds produced by Digital Light Processing using two-step sintering

Claudia Paredes [a,b,*], Jakub Roleček [b], Pedro Miranda [a]

[a] Departamento de Ingeniería Mecánica, Energética y de los Materiales, Universidad de Extremadura, Badajoz, Spain
[b] Central European Institute of Technology, Brno University of Technology, Brno, Czech Republic

ARTICLE INFO

Keywords:
Scaffolds
Calcium phosphate
Mechanical properties
Digital Light Processing
Two-step sintering

ABSTRACT

Digital Light Processing is combined with two-step sintering to obtain bioactive scaffolds with improved strength and mechanical isotropy. Highly loaded photosensitive suspensions were prepared from β-TCP powder to create scaffolds consisting of interpenetrating struts with two different designs. Two sintering methods were used: conventional sintering (*CS*) and two-step sintering (*2SS*). The latter resulted in a microstructure with uniformly shaped grains and reduced porosity. Their compressive strength was determined by uniaxial testing under two different load configurations, with the force applied parallel or perpendicular to the building plane of the scaffolds. Design optimisation and fine-tuning of the sintering process helped in reducing the presence of interlayer defects and minimise the shear-dominated fractures. Isotropic fracture behaviour was achieved, with similar central values of the Weibull distribution (49 ± 1 MPa vs. 51 ± 1 MPa) along both testing directions, showing a great potential for their use in load-bearing bone tissue engineering applications.

1. Introduction

Synthetic bioactive scaffolds have been considered promising candidates for bone replacement as an alternative to grafts and metallic implants for the past 40 years [1–3]. This status is well deserved because of the excellent possibilities they offer. These porous structures are made of materials with excellent biological properties, often ceramics such as calcium phosphates, sulphates, bio-glasses or glass-ceramics that can degrade in contact with body fluids. Among the calcium phosphates, β-tricalcium phosphate (β-TCP) is generally the preferred choice as it can actively promote bone regeneration and has the most appropriate degradation rate [4]. However, despite the numerous research efforts, these porous structures rarely exhibit enough mechanical integrity to provide a reliable clinical solution in load-bearing applications. As ceramics, these materials are intrinsically fragile, and when used for structures with an open pore architecture, which is essential to support bone ingrowth, their mechanical performance is severely compromised. Traditionally, these scaffolds have a Young's modulus and strength that are far below the mechanical performance of the natural bone [3], which limits their suitability for load-bearing areas and would make them extremely difficult for surgeons to handle during implantation.

An important step forward in the fabrication of these structures was achieved by means of additive manufacturing (AM) techniques, i.e., direct ink writing, stereolithography, selective laser sintering, etc., which allow to use ceramics as a feedstock [5]. In contrast to conventional manufacturing techniques, AM technologies allow the fabrication of scaffolds with highly interconnected pores while reducing total volumetric porosity, which can improve their mechanical strength through controlled architecture. Among AM techniques, Digital Light Processing (DLP) allows the fabrication of porous 3D objects with dense and complex strut shapes that can distribute stresses more effectively. Full ceramic parts are obtained from an STL file by photo-curing a resin-based suspension through the action of a UV light source, after undergoing a heat treatment for the elimination of the polymeric resin and posterior sintering [5]. However, DLP-manufactured structures typically have anisotropic fracture responses, with significantly inferior mechanical performance when compressed perpendicularly to their building plane as compared to parallel loading. This is attributed to the presence of interlayer defects that lead to a more shear-dominated fracture, as often observed in laminated ceramic materials tested perpendicular to the lamellae [6,7].

Given the potential of DLP in this area, it is important to make efforts to improve the reliability of objects produced using this technique. To achieve this objective, we propose to take two measures. The first is to

* Corresponding author at: Departamento de Ingeniería Mecánica, Energética y de los Materiales, Universidad de Extremadura, Badajoz, Spain.
E-mail address: clparedes89@unex.es (C. Paredes).

https://doi.org/10.1016/j.jeurceramsoc.2023.11.028
Received 3 October 2023; Received in revised form 9 November 2023; Accepted 11 November 2023
Available online 14 November 2023

use the versatility of the technique to build scaffolds with a strut design that provides better stress distribution and, therefore, reduces the number of shear-dominated fractures. And second, to reduce interlayer defects by improving the densification. Regarding the first approach, several studies have been focused on evaluating the mechanical properties of numerous known structures under compressive loading by means of finite element analysis [8–11]. Among these, the Schwarz Primitive geometry has shown superior performance under compressive stresses than more basic scaffolds consisting of interpenetrating struts of constant square or cylindrical shape, under identical loading conditions and material assumptions, yielding significantly lower stress concentrations that may result in shear-dominated fractures [8]. However, to the best of the author's knowledge, no study has been carried out to manufacture this type of geometry using a ceramic material and subsequently test its mechanical properties, so it is unclear whether it would actually lead to an improvement.

In order to obtain scaffolds with dense struts and to reduce the number of defects generated during sintering, it is necessary to start from suspensions with a high solid content and to carry out an appropriate heat treatment. However, the sintering of β-TCP is a major challenge due to the phase transformations that occur at relatively low temperatures, resulting in cracks formation [12–14]. In this regard, two-step sintering is a promising technique. By employing this sintering approach, it is feasible to obtain a denser material while maintaining the original phase composition and avoiding an excessive grain growth, thus preserving its mechanical strength and integrity. Although several recent studies have addressed the sintering of calcium phosphates by two-step sintering (2SS), especially hydroxyapatite [15–20], their applicability to laminar structures of β-TCP fabricated by DLP remains untested. Therefore, this study focuses on the fabrication using DLP of β-TCP scaffolds with a strut arrangement that enhances their mechanical performance while preserving their biological properties, and with denser, stronger struts through the use of two-step sintering. In order to demonstrate the improvement, the results are compared with those obtained on scaffolds with typical straight strut produced by conventional sintering.

2. Materials and methods

2.1. Fabrication

In a commercially available photopolymer ELEGOO resin (Elegoo, China), consisting of a mixture of 50% epoxy and 40% acrylate functional groups, a 6 wt% of dispersant (DISPERBYK 110, BYK-Chemie GmbH, Germany) was added in order to reduce its initial viscosity and prevent the sedimentation of the subsequently added ceramic powder [21–23]. Photo-sensitive ceramic suspensions with 40 vol% solid loading were obtained using β-TCP powder (Whitlockite OD, Plasma Biotal Ltd., United Kingdom), with an average particle size of 1.84 μm and a density of 3.07 g/cm^3. All components were mixed in a centrifugal planetary mixer THINKY ARE-250 (THINKY, Japan) and the suspension was stored at a temperature of approximately 37 °C to increase the flowability during printing [24].

Three-dimensional modelling was used to create porous scaffolds with an external cubic shape and dimensions of 7.7 × 7.7 × 7.7 mm with two different geometries, both with a designed porosity of 60%. They consisted of a periodical arrangement of cartesian intersecting rounded struts, separated centre-to-centre a distance $s = 1.9$ mm along the three cartesian axes. However, the geometry at the interception between struts varied between the two models as displayed in Fig. 1, which shows the schematic corresponding to a representative unit cell of each of the scaffolds, together with their corresponding dimensions. The simplest scaffold design comprised of repeating the unit cell shown in Fig. 1a, where three cylinders of a constant diameter of 0.9 mm intersect perpendicularly at one point of space. Throughout the manuscript, scaffolds built using this simple cylinder intersection are labelled as ***S***. In

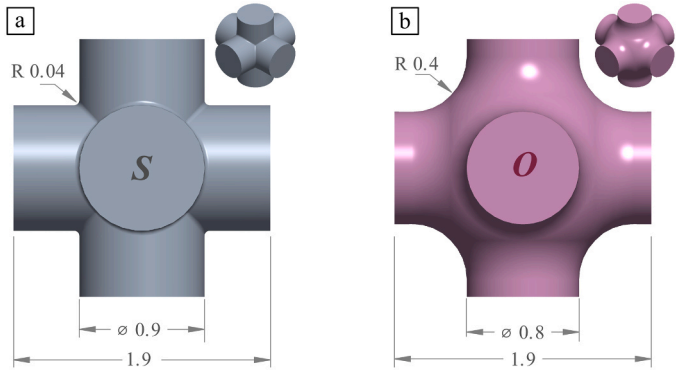

Fig. 1. Schematics of (a) a unit cell corresponding to the simple design with straight struts and sharp intersections, labelled as S, and (b) a unit cell corresponding to the optimised design with smooth intersections, labelled as O. Dimensions in mm are given in both sketches.

the second design (Fig. 1b), rods with a slightly smaller diameter of 0.8 mm intersect in a similar manner but the intersection is rounded to a curvature radius of 0.4 mm to avoid sharp edges. This struts arrangement match a geometry often referred in the literature as Schwarz Primitive [8].

Throughout the text, scaffolds fabricated using this optimised design are labelled ***O***. This design was chosen to mimic the naturally curved surfaces in biological systems to facilitate tissue growth [25–27], to provide better mechanical stability over simpler geometries [8], and to improve the performance of the scaffolds under shear stress [28] due to a more isotropic mechanical response. The 3D models were sliced into 25 μm thick layers and the suspension was loaded into a transparent vat mounted in a bottom-up DLP fabrication system, Prusa SL1 (Prusa Research, Czech Republic). To achieve the required cure depth for each layer, an energy of approximately 13.2 mJ·s/cm^2 was delivered, by exposing the suspension to an UV light at a wavelength of 405 nm and an intensity of approximately 3 mJ/cm^2 for 4.4 s. Post-processing consisted of removal of uncured resin residues using isopropanol, sonication and compressed air. This was followed by a post cure treatment in a UV light chamber for 2 min to reduce the likelihood of defects caused by uneven curing.

2.2. Heat treatment

Debinding was carried out using a two-stage heat treatment including vacuum debinding and removal of residual carbon in the samples from previous pyrolysis. For this, the samples were first placed in a retort furnace (CLASIC 2011DEB, Clasic Ltd., Czech Republic) using a heating profile consisting of two ramps of 0.5 °C/min to 300 °C and 390 °C and a dwell time of 60 min at each temperature, which coincided with the two peaks obtained from a preliminary thermogravimetric analysis. All traces of residual carbon were then eliminated by heating in a conventional furnace (CLASIC 2011DEB, Clasic Ltd., Czech Republic) at 750 °C for one hour at a heating rate of 1 °C/min. For comparison purposes, the resulting green bodies were then sintered using two different strategies: conventional and two-step sintering. Conventional sintering (***CS***) was performed in a conventional chamber furnace (CLASIC 2011DEB, Clasic Ltd., Czech Republic) with a heating rate of 3 °C/min up to 1200 °C and a dwell time of 120 min, while the cooling rate was set to 5 °C/min. On the other hand, two-step sintering (***2SS***) was carried out in a furnace with a bottom loading mechanism (CLASIC 0117E, Clasic Ltd., Czech Republic). This furnace allowed the controlled transfer of the samples into a preheated hot zone located in the upper part of the furnace. Specifically, three different heating profiles were used. All profiles shared the same heating and cooling rates, 100 °C/min controlled by the speed of platform movement, as well as the dwell time, 180 min, and the temperature of the second stage, $T_2 = 1000$ °C. On the

contrary, the first stage varied between them as follows. The first profile consisted of a first stage at T_1 with a dwell time of 2 min, in the second profile the dwell was reduced to 1 min and in the third profile the samples reached the T_1 and were immediately cooled. Scaffolds treated under these conditions were marked as ***2SS-2***, ***2SS-1*** and ***2SS-0***, respectively. In addition, in order to achieve the best microstructure, i.e., the maximum densification in each condition without excessive grain growth, different peak temperatures (T_1) were used in each condition. Table 1 summarises all parameters for the heat treatments.

2.3. Microstructural characterisation

The initial phase-composition of the powder and the final crystalline phases present in the samples subjected to the sintering treatments were identified by X-ray diffractometry (Rigaku SmartLab 3 kW, Rigaku, Japan) on powder obtained by crushing the sintered specimens. The diffractometry was performed at a voltage of 40 kV and a current of 30 mA, in the Bragg-Brentano measuring mode between 10° and 90°, with a scanning speed of 3°/min. A Rietveld analysis was performed using MAUD (Material Analysis Using Diffraction) software [29] and the structural models corresponding to α-TCP and β-TCP published in the Crystallography Open Database [30–32] to estimate the amount of each phase. The external dimensions of the samples were measured after printing and subsequent sintering using a digital calliper to evaluate the shrinkage suffered after each treatment, and their apparent density was calculated by also measuring their weight in a digital balance. Although the macroporosity of the scaffolds was designed to be 60%, deviations from the original model are likely to occur due to light scattering and overexposure. Therefore, the struts and pore dimensions were measured by optical microscopy in order to calculate their actual porosity. Finally, scanning electron microscopy (TESCAN LYRA3, TESCAN Brno Ltd., Czech Republic) was used to observe the sample's struts shape, surface quality and microstructure, as well as to estimate their grain size. Average grain size values were obtained by Gauss fitting from more than 400 grain measurements.

2.4. Mechanical testing

The compressive strength (σ_c) was determined from the maximum load observed during uniaxial compression tests performed on a minimum of 10 sintered specimens per sample design. The tests were performed on a universal testing machine, specifically the Shimadzu Autograph AG-IS. The specimens were loaded either perpendicular (⊥) or parallel (∥) to the building plane at a constant crosshead speed of 0.6 mm/min.

3. Results

3.1. Microstructural characterisation

The SEM micrographs shown in Fig. 2 were taken on polished and thermally etched surfaces of the scaffolds after each heat treatment profile at different peak temperatures, as indicated. In particular, the left column of this figure contains an image corresponding to a conventionally sintered scaffold at 1200 °C (Fig. 2a) and two-step sintered scaffold sintered at: 1250 °C using the heating profile *2SS-2* (Fig. 2d), 1270 °C using the *2SS-1* profile (Fig. 2g), and 1290 °C using the *2SS-0* profile (Fig. 2j). Differences in the resulting microstructure after each treatment are evident, particularly when comparing the conventionally sintered samples with the two-step sintered ones. The microporosity of the struts was reduced gradually as the sintering temperature increased for each heat treatment profile. For example, for the left column samples, 5.3 ± 0.3% porosity remained after conventional sintering, but this value decreased to 2.2 ± 0.3%, 2.9 ± 0.4% and 0.18 ± 0.02% after each two-step sintering condition. In parallel, although the peak sintering temperatures were increased, the reduction in the dwell time allowed reducing the grain growth. In particular, the average grain size decreased from 3.3 ± 0.1 μm for conventional sintering to 2.2 ± 0.1 μm, 1.83 ± 0.03 μm and 1.73 ± 0.05 μm for two-step sintering, using the *2SS-2*, *2SS-1*, and *2SS-0* lower temperature profiles, respectively.

Although the peak sintering temperatures in each case were above 1115–1160 °C, where a phase transformation (β→α) is known to occur in stochiometric TCP [33,34], the microstructures of the scaffolds did not exhibit any traces of second phases or cracks associated with phase transformations (see Fig. 2a, d, g, and j). However, this is not the case of the micrographs in the middle column of the Fig. 2 (Fig. 2b, e, h, and k), showing scaffolds sintered with the same heating profile as aforementioned counterparts, but with the peak temperature 30 °C higher, in the case of conventional sintering, and 20 °C higher for all two-step sintered scaffolds. This minor temperature increase was sufficient to induce the appearance of cracks throughout the whole volume of the scaffolds due to internal stresses in the material resulting from the volumetric changes in the crystal lattice during the β↔α phase transformations [13,35]. Interestingly, a bimodal grain size distribution appeared in the microstructure of the two-step sintered scaffolds, regardless of the sintering profile used. Abnormal grain growth, as evidenced by the microstructures shown in Fig. 2e, h, and k, has been already reported in several studies when sintering β-TCP with a Ca/P ratio lower than 1.5, often related to presence of calcium pyrophosphate (CPP) [36,37]. In this situation, and in a accordance with the CaO-P_2O_5 diagram, a liquid phase is formed at temperatures above 1280 °C, causing abnormal grain growth [14,38,39]. As the peak sintering temperatures depicted in the left column of Fig. 2 were the highest temperatures that avoided this excessive grain growth or cracking, they were considered to be the optimal for each sintering profile. Therefore, the *2SS-0* sintering profile, with the peak temperature of 1290 °C in the first stage, appears to be the best sintering treatment to this point. The microstructure shows uniformly shaped grains of the same size as those sintered at lower temperatures with other heating profiles but exhibiting the lowest number of pores.

The phase composition of the scaffolds sintered at the higher temperatures for all sintering profiles was analysed by X-ray diffraction and the resulting patterns are also shown in Fig. 2 (2c, f, i and l). Although the microstructure of these scaffolds showed numerous cracks, and in the case of *2SS* samples also a bimodal grain size distribution, which could be interpreted as evidence of the appearance of a second phase, the only crystalline phase identified in all of them, regardless the sintering profile, was β-TCP. In the case of conventional sintering of stochiometric β-TCP, it would be likely that during the two-hour dwell time a significant portion of the initial powder underwent a transformation to α-TCP. It could be argued that the presence of a small amount of CPP [37] (below 3%, and therefore difficult to detect by XRD) may have influenced its compositional behaviour, stabilising the β-phase during sintering above these temperatures [37,39]. However, the generation of cracks indicates the occurrence of β→α phase transformation in a significant portion of material during sintering, followed most likely by the reverse (α→β) transformation during cooling, given the slow cooling rate employed [33,34] and the possible presence of CPP, which can

Table 1
Heat treatments used in conventional sintering (CS) and two-step sintering (2SS) with corresponding dwell times.

Label	Heating /cooling rate [°C/min]	T1 [°C]	Dwell [min]	T2 [°C]	Dwell [min]
CS	3 / 5	1200 / 1230	120	-	-
2SS-2	100 / 100	1250 / 1270	2	1000	180
2SS-1		1270 / 1290	1		
2SS-0		1290 / 1310	0		

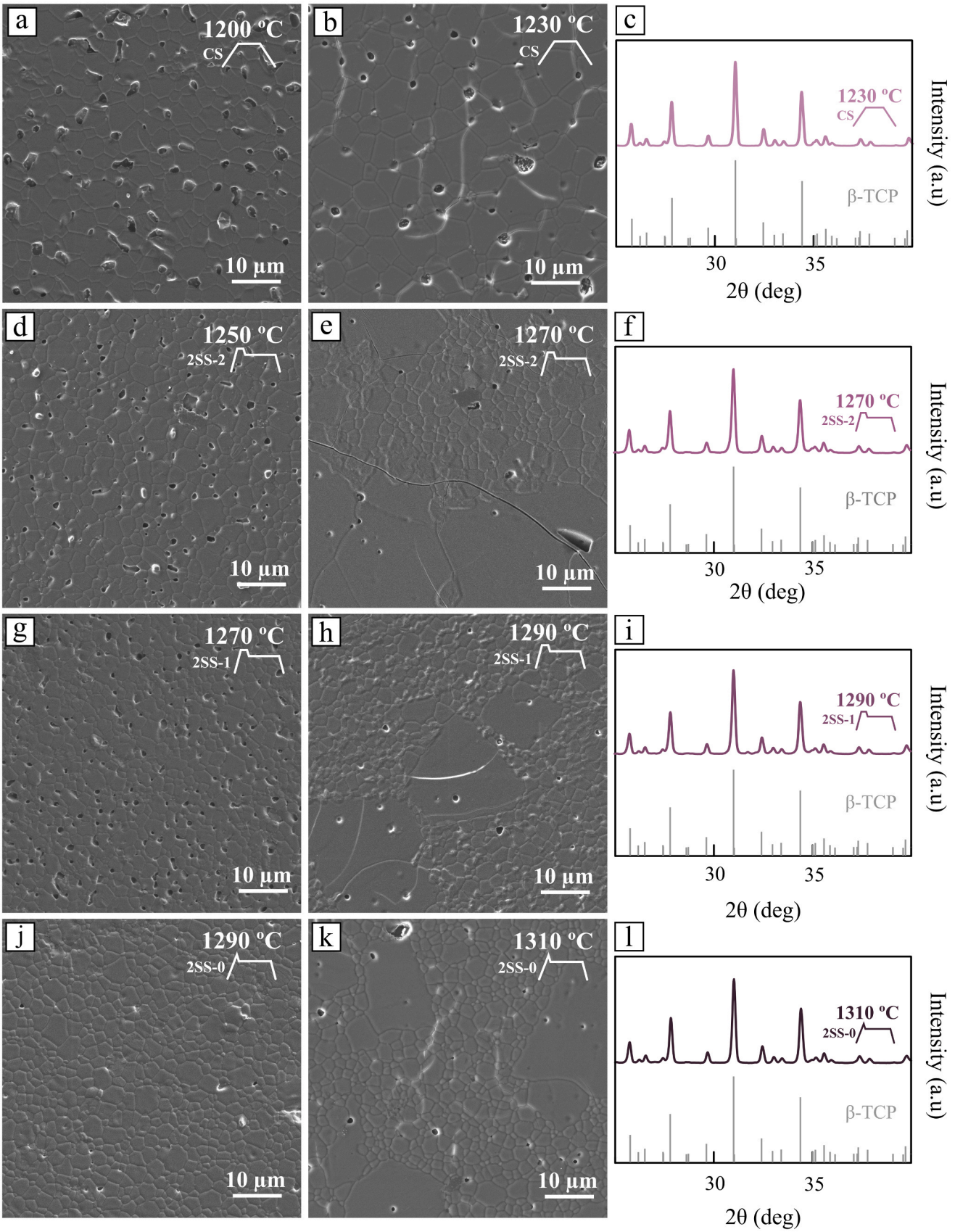

Fig. 2. SEM cross-sectional micrographs of polished and thermally etched surfaces of samples (a, b) conventionally sintered at 1200 and 1230 °C, and using two-step sintering with a plateau and temperature in the first stage of (d, e) 2 min at 1250 and 1270 °C, (g, h) 1 min at 1270 and 1290 °C, and (j, k) 0 min at 1290 and 1310 °C as indicated in the legend and corresponding XRD patterns (c, f, i and l). Standard XRD pattern of pure β–TCP [31] is included for comparison.

promote this reverse transformation [37].

Even though the peak temperatures reached in the first stages of the three 2SS sintering profiles would be sufficient to induce β→α phase transformation and the subsequent rapid-cooling rate should have limited the reverse transformation, again in a stochiometric situation, the short dwell times together with the calcium deficiency in the starting powders could be responsible for the prevalence of the β-phase. However, given the presence of cracks in their microstructure due to internal residual stresses, mainly within the larger grains, it is likely that the phase transformation occurred indeed. This would indicate that the reverse α→β transformation may have taken place during the second step of the sintering performed at 1000 °C. The prevalence of the β-TCP phase was already observed in a previous study [12] concerning the sintering of β-TCP using rapid sintering technique consisting of only one step with a longer dwell time (5 min) at 1300 °C and above, proving the need for long dwell times to achieve a persistent the β→α transformation. Although the Ca/P ratio in the starting powder appears to be different between the two studies, given the absence of a liquid phase even at higher sintering temperatures in the previous work, the results are consistent. In fact, a lower Ca/P ratio in the powder would hinder β→α transformation, as the temperature required for the transformation to occur is slightly higher [37].

Given the good results obtained with *2SS-0* sintering profile with a peak temperature of 1290 °C in terms of microstructure and phase composition, this profile was chosen for two-step sintering of our scaffolds. Scaffolds sintered by conventional sintering at 1200 °C for 2 h were chosen for further comparison. In order to analyse first the influence of the design and then the improvement that the optimised treatment has brought to the mechanical properties of the scaffolds, conventional sintering was used to treat both *S* and *O*-specimens. An additional batch of *O*-scaffolds was sintered using the optimal two-step sintering profile. Images corresponding to the unit cell of the three mentioned types of fabricated scaffolds are shown in Fig. 3, as labelled. Unlike in the original 3D model, the edges of the struts facing us in the image are rounded due to the limited tolerance of the printer and the UV light dispersion caused by the ceramic particles. This causes some certain rounding at the corners of the rod intersections and an overall increase in the actual cured area. Measurements of strut and macro-pore dimensions of the green bodies indicated that the light scattering was responsible for reducing the designed macroporosity from 60% to ≈ 52%. As for their surface appearance, although it is generally good regardless of the heat treatment they have undergone, some defects can be observed. Firstly, it is easy to distinguish the individual building layers, which is a typical feature of DLP-made structures. Along the struts, it is sometimes possible to observe some discontinuities in the form of small depressions and bumps. These could have been caused during the printing process by improper mixing of the suspension, either by a lack of ceramic particles in the first case or by its agglomeration in the second case, trapping some particles outside the intended curing area. However, both defects could also have occurred during the removal of the organic material (debinding).

Nevertheless, as can be seen in Fig. 4a and b, both samples demonstrate good adhesion between the printing layers and there are no visible traces of interlayer defects on the polished inner surface. However, the transition between layers becomes considerably smoother in the case of two-step sintering process. For the conventionally sintered scaffolds, the measured shrinkage values were 21 ± 1% in the *xy* direction and 23 ± 1% in the *z* direction, while for the two-step sintered scaffolds, these values increased to 23 ± 1% and 24 ± 1%, respectively. As intended, the apparent densities of the conventionally sintered scaffolds were very similar for both designs with values of 1.31 ± 0.05 g/cm^3 and 1.32 ± 0.02 g/cm^3 for *S* and *O* respectively. The *O* scaffolds sintered by two-step sintering reached an apparent density of 1.40 ± 0.03 g/cm^3. Therefore, the improvement in the densification produced by 2SS can be quantified to be approximately 6%. Considering the calculated macroporosity and the theoretical density values this indicates that struts relative density increased from roughly 90% in conventionally sintered scaffolds to almost full densification (≥ 96%) in 2SS sintered specimens. These estimates are also in good agreement with the SEM observations on the fracture surfaces of both specimens. While the conventionally sintered scaffold (Fig. 4c) has a significant number of pores along the strut, the number of pores in the fracture surface of the 2SS-0 scaffold (Fig. 4d) is minimal, with hardly any visible. The effectiveness of such a short 2SS treatment in achieving full densification of the scaffold struts has probably been favoured by the open architecture of the scaffolds and the relatively small dimensions of the struts. Indeed, these features facilitate the achievement of a uniform microstructure throughout the scaffolds, despite minimising the time the material is exposed to the peak temperature, and thus reducing the negative effects (grain growth, phase transformation to α-TCP, internal stresses, microcracking, etc.) that longer dwell times would cause. Fabrication of large bulk samples by this methodology may prove more difficult and could lead to uneven densification of the part, with denser surface and more porous cores. This may generate deleterious internal stresses, negating some of the benefits achieved by 2SS, although such extreme should be verified experimentally in follow-up studies. In any case, none of this is of concern in the fabrication of porous scaffolds, which is the objective of this work.

3.2. Mechanical characterisation

Uniaxial compression tests were carried out to evaluate the behaviour of each specimen under compressive stress by applying a force either perpendicular (⊥) or parallel (||) to the building plane. These tests aimed to identify the strongest design and the more damaging load configuration mode, respectively. Representative stress (σ) – strain (ε)

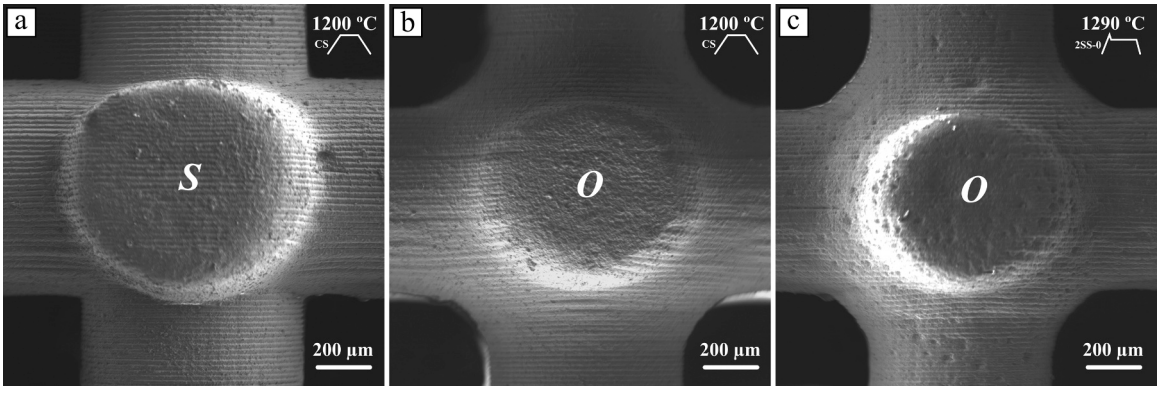

Fig. 3. Representative SEM micrographs of the lateral surface of struts corresponding to scaffolds sintered as indicated on the labels and oriented with the first printed layer at the bottom.

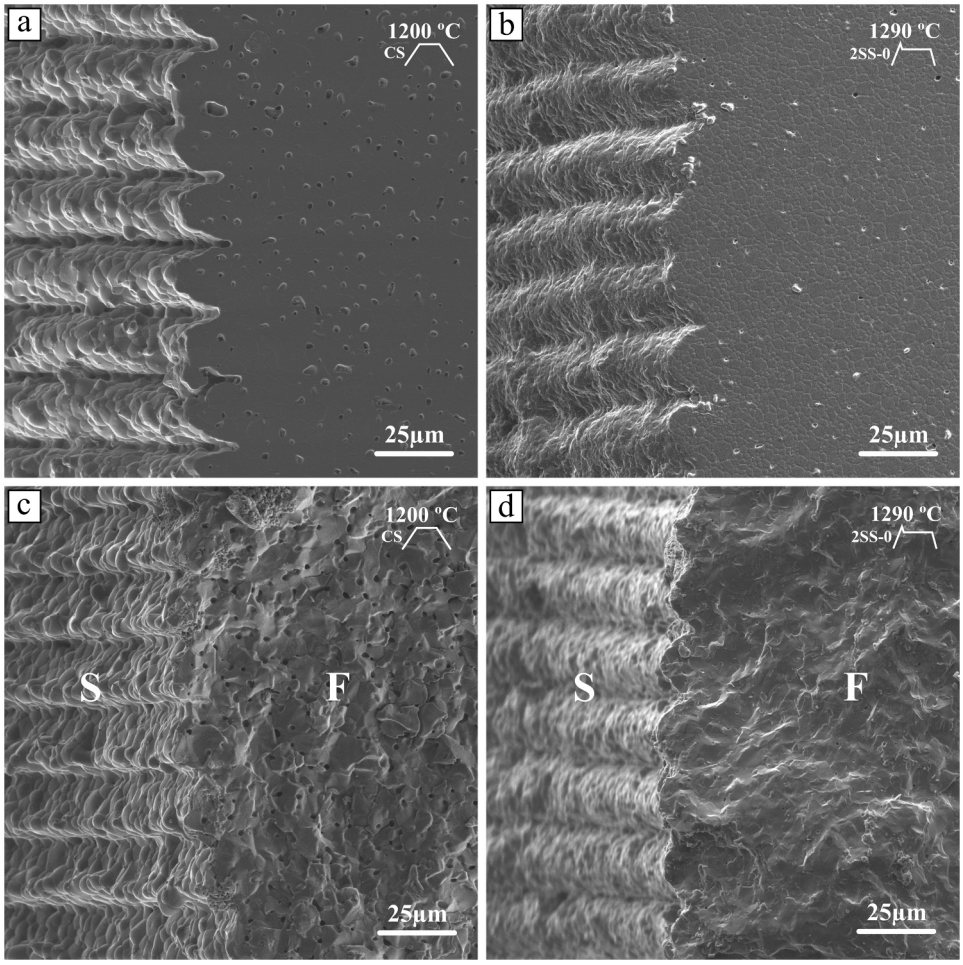

Fig. 4. Representative SEM micrographs of the lateral surface of struts and corresponding polished (a, b) and fracture (c, d) cross-sections of scaffolds thermally etched and sintered as indicated in the legend.

curves resulting from these compression tests performed on *S* and *O*-specimens sintered in a conventional furnace are included in Fig. 5. These curves indicate that all scaffolds exhibited brittle behaviour: once the maximum stress was reached, the curves dropped to zero after very short strains, whether tested perpendicular or parallel to the printing plane. However, the performance of the optimised scaffolds with the Schwartz Primitive geometry reached the maximum strength with little sign of any previous damage to the structure, in contrast to scaffolds made of straight struts with intersecting edges, which showed more serrated curves, especially when tested with the load perpendicular to

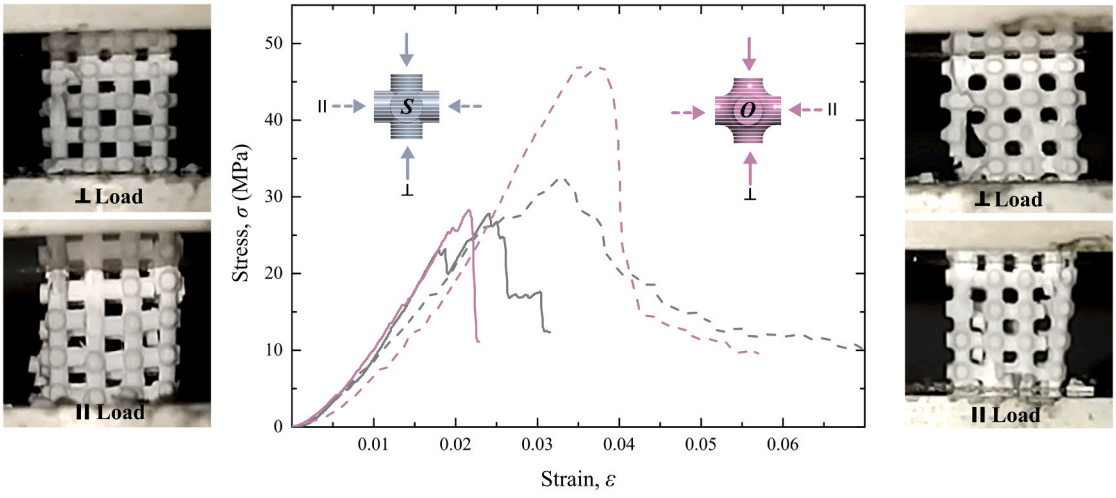

Fig. 5. Stress-strain curves and images captured in-situ during uniaxial compression tests performed on scaffolds of struts with intersecting edges on the left (S) and with optimised geometry on the right (O), as indicated in the legend.

the printing plane. These results are in a good correlation with previous reports on laminated structures [6,7,12,40].

Images on the sides of the graph in Fig. 5 illustrate the differences in the fracture mode observed in situ during the tests on each type of specimens. On the left there are two images corresponding to scaffolds with straight struts and intersecting edges: multiple cracks appear at different locations on the scaffolds, always close to the intersection of the struts. When tested perpendicularly, cracks grow at a 45° angle from the applied load, indicating a shear dominated fracture propagating through interlayer defects. Fracture occurs indistinctly through either of the two horizontal rod orientations. However, under parallel loading, the cracks propagate predominantly through the interlayers so fractures appear vertical and occur preferentially along the printing plane, i.e., favouring one of the two horizontal directions. The right-side images one Fig. 5, corresponding to tests carried out on scaffolds with optimised design, show a similar preferential fracture along the interlayers, but crack initiation is displaced away from the intersection towards the centre of the freestanding segments of the rods. This is especially evident when subjected to a parallel load, where cracks form somewhere near the thinnest diameter of the strut and propagates perpendicularly between the fabrication layers.

The different mechanical performance of both designs is evidenced in the Weibull plot in Fig. 6a, which shows the failure probability as a function of applied compressive stress. The straight solid (⊥) and dashed (||) lines, are the best fits to experimental data using the Weibull probability function, $P = 1 - e^{[-(\sigma/\sigma_0)^m]}$ [41], where P is the probability of failure and the adjustable parameters m and σ_0, are the Weibull modulus and the central value, respectively. According to this figure, the reliability of scaffolds with straight struts remained low independently of the load configuration, with a Weibull modulus of 5.8 ± 0.5 and 5.3 ± 0.4 in perpendicular and parallel configurations, respectively. Conversely, the reliability of the optimised geometry scaffolds increased significantly when tested under a parallel load configuration, exhibiting a Weibull modulus of 10.2 ± 0.9, compared to 4.2 ± 0.2 for a perpendicular load. Additionally, in Fig. 6b, the compressive strength (evaluated as the central value, σ_0, of the Weibull distribution) measured for these scaffolds is represented. Although the performance of all scaffolds was superior to trabecular bone [42], clear differences are observed between the different designs and load configurations.

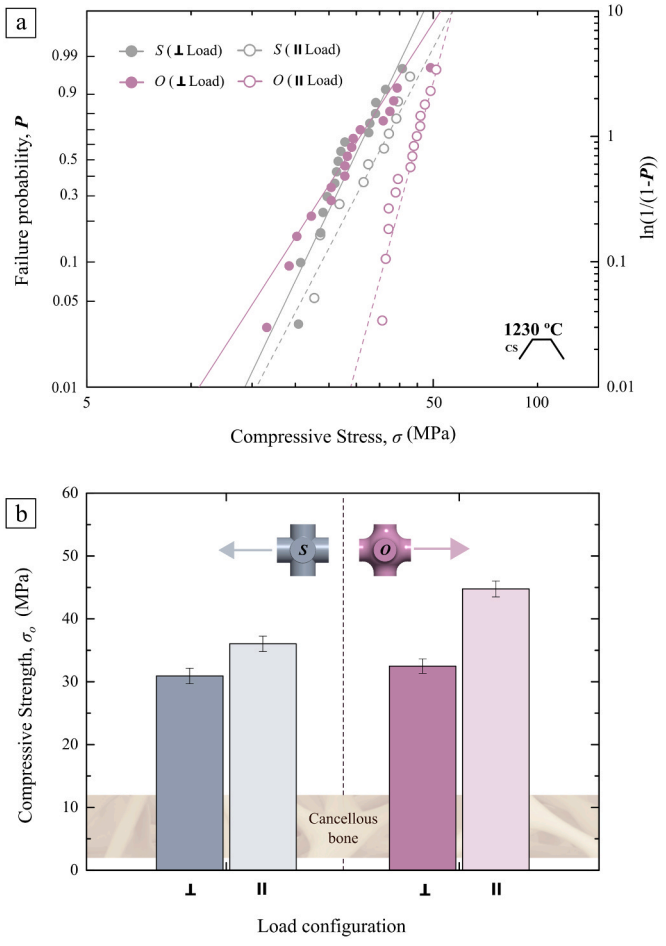

Fig. 6. (a) Weibull compressive strength plot (i.e., failure probability vs. applied stress). The straight lines are linear fits to data using a Weibull probability function. (b) Weibull central values (σ_0) for S and O scaffolds sintered conventionally at 1230 °C. Error bars represent standard errors in the estimation of σ_0 and are not related to strength data scattering.

When the scaffolds were tested under perpendicular loads, the strength was very similar for both designs, although slightly superior for scaffolds with optimised design (33 ± 1 MPa vs 31 ± 1 MPa for scaffolds with straight struts). The differences became more obvious when tested in a parallel configuration, reaching 36 ± 1 MPa and 45 ± 1 MPa for the *S* and *O* scaffolds, respectively. The difference in strength observed between loading modes as well as in the observed fracture patterns indicates that DLP scaffolds, regardless of their design have a different predominant fracture mode depending on whether the load is applied perpendicular or parallel to their printing plane [6,7]. When tested perpendicularly, fracture is dominated by in-plane shear stresses (mode II), while in parallel the orientation of the weaker interlayers favours a mode I fracture. Although it was expected that *O* scaffolds would perform better than *S* scaffolds when tested perpendicularly, since the Schwartz Primitive geometry should alleviate shear stresses compared to simpler geometries with intersecting edges [9,28], this is true depending on the level of macroporosity and for the actual values obtained here (~50%) the maximum shear stresses are quite similar in both designs [8]. Therefore, the change in design fails to improve significantly the performance of the scaffolds when tested perpendicularly. However, the *O* design succeeds in reducing the concentration of tensile stresses generated at the intersection between struts by smoothing those corners, thus hampering the generation of fissures when tested in parallel configuration. The significantly increased reliability (increased slope in Fig. 6a) observed in the *O* scaffolds in this case may also be related to this rounding of the intersections which increases the area over which the higher tensile stresses in the structure are distributed, which decreases scattering in the strength data [43].

Given the superior performance of the *O* scaffolds, this design was selected to evaluate the effect of two-step sintering in the scaffolds' mechanical performance under compressive stresses. Fig. 7a shows the Weibull plots corresponding to scaffolds sintered in two steps with a peak temperature of 1290 °C (*2SS-0*). The data are represented by solid symbols when tested under perpendicular load configuration and by hollow symbols for parallel loading, and the best fits using the Weibull probability function are represented by straight solid (⊥) and dashed lines (||). From these results it is evident that the mechanical performance of the scaffolds with the optimised geometry and sintered by two-step sintering was largely independent of the loading orientation. The isotropic behaviour was not limited to the similar distribution of compressive strength values—central values of the Weibull distribution were 49 ± 1 MPa in the perpendicular direction and 51 ± 1 MPa in the parallel direction, and the Weibull modulus 4.3 ± 0.5 and 3.9 ± 0.1, respectively— but also in the fracture mode. In situ observations during the tests and on post-mortem examination of resulting debris did not show any evidence of shear-dominated fracture in the scaffolds tested under perpendicular loads. Thus, fracture mode appeared to be similar under both loading configurations. These results indicate that improving densification is essential to minimise interlayer defects and achieve an isotropic response in DLP-printed objects. Compressive strength values were significantly larger than in conventionally sintered structures, even

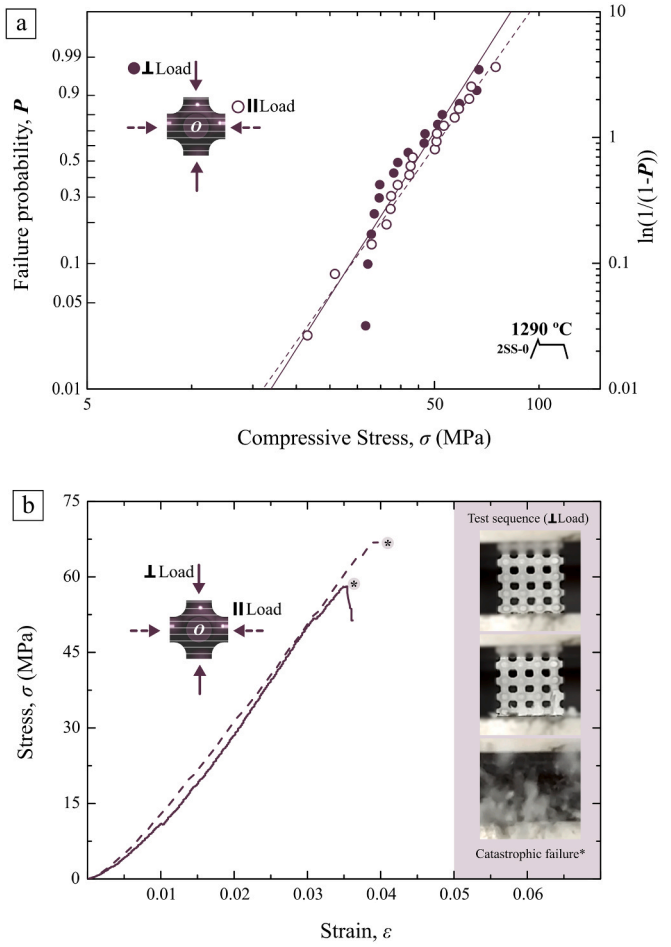

Fig. 7. (a) Weibull compressive strength plot (i.e., failure probability vs. applied stress) for O scaffolds produced by two-step sintering with a plateau and temperature in the first stage of 0 min at 1290 °C and 180 min at 1000 °C, tested in perpendicular and parallel loading configurations. The straight lines are linear fits to data using a Weibull probability function. (b) Representative stress-strain curves and sequential images frames captured in-situ at peak load during the tests to illustrate the catastrophic and abrupt failure.

those tested in parallel configuration and fracture was, consequently, more abrupt and catastrophic, as shown in Fig. 7b.

Rarely any secondary fracture events were observed before peak load was reached, and when they did appear location of fracture was always close to the contacts with the compression plates. The higher elastic energy released upon fracture resulted in a violent failure of the scaffolds with multiple pieces bursting off the specimen and a sudden load drop to zero, very unlike the progressive fracture and load decrease observed in conventionally sintered scaffolds (Fig. 5). The catastrophic nature of failure and the subsequent increased role of contact irregularities on the experimental results obtained during the tests are considered the most probable reason for the large scattering in the strength data and the relatively poor reliability of these optimised samples. However, it could also be possible that the fast heating and cooling rates used in 2SS may lead to intrinsic variabilities in the defect populations of the fabricated scaffolds that might explain as well their relatively low Weibull modulus.

Fig. 8 shows a plot of the strength achieved by the scaffolds as a function of material density on the bottom axis, and the scaffold's total porosity on the top axis. These values are compared with analogous results for DLP fabricated β-TCP scaffolds obtained in our previous studies [7,12,44,45], as well as with values for β-TCP scaffolds manufactured by DLP or by Direct Ink Writing (DIW, also known as

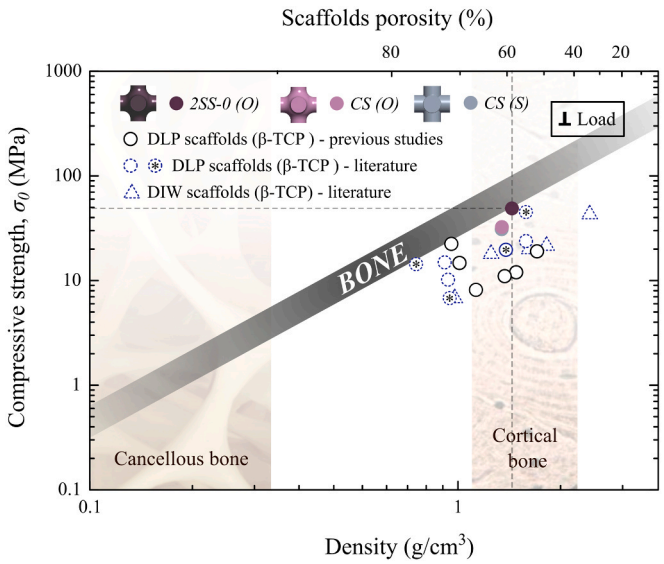

Fig. 8. Comparative plot of compressive strength for scaffolds fabricated in this study, our previous works [7,12,44,45] and literature reports [40,46–51] of β-TCP scaffolds fabricated by DLP or by DIW, as indicated in the legend. The load configuration in the data marked with (*) is undefined [40]. The results are plotted as a function of material density. The shaded band represents bone properties (including data dispersion) as a function of apparent bone dry density, estimated using an empirical power law model from T.S. Keller [48,52].

robocasting) obtained from literature [40,46–51]. In addition, all these values are compared to estimated values for human bone tissue following the empirical model of Keller [48,52], represented, with its corresponding data dispersion, as a shaded band in the figure. Note that in the Fig. 8 for the compressive strength data marked in the legend with (*), the load configuration was not specified within the study [40], and thus the values could be overestimated. The results show that the β-TCP scaffolds with optimised geometry produced by two-step sintering exhibited the highest strength values, approaching the performance of cortical bone with the same dry density. This highlights the importance of the optimisation approaches proposed in this work towards achieving mechanically sound calcium phosphate scaffolds that may eventually allow the production of reliable bone graft substitutes for load bearing regions of the skeleton.

4. Conclusions

In this study, porous scaffolds were fabricated using Digital Light Processing from β-TCP as the starting material. This technique allowed the fabrication of scaffolds consisting of intersecting struts with either sharp (*S*) or smooth (*O*) intersections, while maintaining the same porosity. After conventional sintering, both designs were evaluated by uniaxial compression testing using different configuration loads. As a result, both designs performed better when tested in a parallel configuration, with cracks showing tangential displacements when tested in a perpendicular configuration. Weibull statistics were used to compare the strength of the two designs, with the central value, σ_0, of distribution being circa 8–20% higher for the scaffolds with the improved geometry in perpendicular and parallel configurations, respectively.

A two-step sintering technique with different peak temperatures and dwell times was introduced to minimise the presence of defects and porosity in the struts. The XRD spectra showed that it was possible to use peak temperatures above 1200 °C for a short time (between 0 and 2 min) without inducing phase transformations. Of all the conditions studied, a sintering profile with a peak temperature of 1290 °C and 0 min dwell yielded the best microstructure, with uniformly shaped, fine grains and lowest remaining porosity. Compared to conventional

sintering, grain size and porosity have been reduced by approximately 50%. These improvements helped to reduce the presence of interlayer defects and therefore the number of shear-dominated fractures, which directly increased the strength of the scaffolds when tested under perpendicular loading. However, when the sintering conditions were slightly varied, either the densification improvement was not sufficient or cracks and abnormal grain growth were observed along the microstructure.

In this way, with two-step sintering technique, it is possible to obtain layered scaffolds with an isotropic response under compressive stress, i.e., independent of the load configuration. Furthermore, this sintering strategy, combined with the use of an appropriate design, makes it possible to obtain bioactive scaffolds with a compressive strength comparable to that of cortical bone of the same dry density. Although further research and investigation would be required to obtain a more extensive mechanical analysis—e.g., by evaluating their performance under bending stresses— and to increase the reliability of the material, the β-TCP scaffolds obtained in this work were already found to have excellent mechanical performance in terms of strength. This suggests that there is a great potential for scaffolds produced in this way to be used in load-bearing applications in bone tissue engineering.

CRediT authorship contribution statement

Claudia Paredes: Conceptualization, Methodology, Investigation, Writing – original draft, Funding acquisition. **Jakub Roleček:** Conceptualization, Methodology, Resources, Writing – review & editing. **Pedro Miranda:** Conceptualization, Resources, Supervision, Writing – review & editing, Funding acquisition.

Declaration of Competing Interest

The authors declare that they have no known competing financial interests or personal relationships that could have appeared to influence the work reported in this paper.

Acknowledgements

CzechNanoLab project LM2023051 funded by MEYS CR is gratefully acknowledged for the financial support of the measurements/sample fabrication at CEITEC Nano Research Infrastructure. Similarly, ENAMEL project, Grant PID2021-123218OB-I00 funded by MCIN/AEI/10.13039/501100011033 and ERDF A way of making Europe, is gratefully acknowledged for the financial support of the measurements performed at University of Extremadura.

Claudia Paredes acknowledges support from the Spanish Ministerio de Universidades through the programme Margarita Salas para la Formación de Jóvenes Doctores (MS-2), funded by the European Union NextGenerationEU/PRTR.

References

[1] M.P. Nikolova, M.S. Chavali, Recent advances in biomaterials for 3D scaffolds: a review, Bioact. Mater. 4 (2019) 271–292, https://doi.org/10.1016/j.bioactmat.2019.10.005.

[2] S.V. Dorozhkin, Calcium orthophosphates as bioceramics: state of the art, J. Funct. Biomater. 1 (2010) 22–1074, https://doi.org/10.3390/jfb1010022.

[3] D.W. Hutmacher, J.T. Schantz, C.X.F. Lam, K.C. Tan, T.C. Lim, State of the art and future directions of scaffold-based bone engineering from a biomaterials perspective, J. Tissue Eng. Regen. Med. 1 (2007) 245–260, https://doi.org/10.1002/term.24.

[4] G. Daculsi, O. Laboux, O. Malard, P. Weiss, Current state of the art of biphasic calcium phosphate bioceramics, J. Mater. Sci. Mater. Med. (2003) 195–200, https://doi.org/10.1023/A:1022842404495.

[5] N. Travitzky, A. Bonet, B. Dermeik, T. Fey, I. Filbert-Demut, L. Schlier, T. Schlordt, P. Greil, Additive manufacturing of ceramic-based materials. Advanced Engineering Materials, Wiley-VCH Verlag,, 2014, pp. 729–754, https://doi.org/10.1002/adem.201400097.

[6] P. Feng, X. Meng, J.F. Chen, L. Ye, Mechanical properties of structures 3D printed with cementitious powders, Constr. Build. Mater. 93 (2015) 486–497, https://doi.org/10.1016/j.conbuildmat.2015.05.132.

[7] C. Paredes, F.J. Martínez-Vázquez, H. Elsayed, P. Colombo, A. Pajares, P. Miranda, Evaluation of direct light processing for the fabrication of bioactive ceramic scaffolds: Effect of pore/strut size on manufacturability and mechanical performance, J. Eur. Ceram. Soc. 41 (2021) 892–900, https://doi.org/10.1016/j.jeurceramsoc.2020.09.002.

[8] J. Shin, S. Kim, D. Jeong, H.G. Lee, D. Lee, J.Y. Lim, J. Kim, Finite element analysis of Schwarz P surface pore geometries for tissue-engineered scaffolds, Math. Probl. Eng. 2012 (2012), https://doi.org/10.1155/2012/694194.

[9] Z. Chen, Y.M. Xie, X. Wu, Z. Wang, Q. Li, S. Zhou, On hybrid cellular materials based on triply periodic minimal surfaces with extreme mechanical properties, Mater. Des. 183 (2019), https://doi.org/10.1016/j.matdes.2019.108109.

[10] T. Bhardwaj, S.P. Singh, M. Shukla, Finite element modeling and analysis of implant scaffolds, in: Proceedings of the International Conference on Advances in Mechanical, Industrial, Automation and Management Systems, AMIAMS 2017, 2017, pp. 358–362, doi: 10.1109/AMIAMS.2017.8069239.

[11] P. Miranda, A. Pajares, F. Guiberteau, Finite element modeling as a tool for predicting the fracture behavior of robocast scaffolds, Acta Biomater. 4 (2008) 1715–1724, https://doi.org/10.1016/j.actbio.2008.05.020.

[12] C. Paredes, J. Roleček, L. Pejchalová, T. Spusta, D. Salamon, P. Miranda, Evaluating the suitability of fast sintering techniques for the consolidation of calcium phosphate scaffolds produced by DLP, J. Eur. Ceram. Soc. 43 (2023) 6493–6503, https://doi.org/10.1016/j.jeurceramsoc.2023.05.052.

[13] F.H. Perera, F.J. Martínez-Vázquez, P. Miranda, A.L. Ortiz, A. Pajares, Clarifying the effect of sintering conditions on the microstructure and mechanical properties of β-tricalcium phosphate, Ceram. Int. 36 (2010) 1929–1935, https://doi.org/10.1016/j.ceramint.2010.03.015.

[14] E. Champion, Sintering of calcium phosphate bioceramics, Acta Biomater. 9 (2013) 5855–5875, https://doi.org/10.1016/j.actbio.2012.11.029.

[15] Y. Zeng, Y. Yan, H. Yan, C. Liu, P. Li, P. Dong, Y. Zhao, J. Chen, 3D printing of hydroxyapatite scaffolds with good mechanical and biocompatible properties by digital light processing, J. Mater. Sci. 53 (2018) 6291–6301, https://doi.org/10.1007/s10853-018-1992-2.

[16] P. Feng, M. Niu, C. Gao, S. Peng, C. Shuai, A novel two-step sintering for nano-hydroxyapatite scaffolds for bone tissue engineering, Sci. Rep. 4 (2014), https://doi.org/10.1038/srep05599.

[17] M. Mazaheri, M. Haghighatzadeh, A.M. Zahedi, S.K. Sadrnezhaad, Effect of a novel sintering process on mechanical properties of hydroxyapatite ceramics, J. Alloy. Compd. 471 (2009) 180–184, https://doi.org/10.1016/j.jallcom.2008.03.066.

[18] M. Lukić, Z. Stojanović, S.D. Škapin, M. Maček-Kržmanc, M. Mitrić, S. Marković, D. Uskoković, Dense fine-grained biphasic calcium phosphate (BCP) bioceramics designed by two-step sintering, J. Eur. Ceram. Soc. 31 (2011) 19–27, https://doi.org/10.1016/j.jeurceramsoc.2010.09.006.

[19] I.Y. Kim, J. Wen, C. Ohtsuki, Fabrication of α-tricalcium phosphate ceramics through two-step sintering, Key Eng. Mater. 631 (2014) 78–82, https://doi.org/10.4028/www.scientific.net/kem.631.78.

[20] A. Indurkar, R. Choudhary, K. Rubenis, J. Locs, Advances in sintering techniques for calcium phosphates ceramics, Materials 14 (2021) 1–18, https://doi.org/10.3390/ma14206133.

[21] P. Sokola, M. Kalina, J. Smilek, P. Ptáček, J. Krouská, D. Salamon, T. Spusta, Kinetic stability and rheological properties of photosensitive zirconia suspensions for DLP printing, Ceram. Int. 49 (2023) 18502–18509, https://doi.org/10.1016/j.ceramint.2023.02.223.

[22] X. Xu, S. Zhou, J. Wu, C. Zhang, X. Liu, Inter-particle interactions of alumina powders in UV-curable suspensions for DLP stereolithography and its effect on rheology, solid loading, and self-leveling behavior, J. Eur. Ceram. Soc. 41 (2021) 2763–2774, https://doi.org/10.1016/j.jeurceramsoc.2020.12.004.

[23] R. Gmeiner, G. Mitteramskogler, J. Stampfl, A.R. Boccaccini, Stereolithographic ceramic manufacturing of high strength bioactive glass, Int. J. Appl. Ceram. Technol. 12 (2015) 38–45, https://doi.org/10.1111/ijac.12325.

[24] V. Tomeckova, J.W. Halloran, Flow behavior of polymerizable ceramic suspensions as function of ceramic volume fraction and temperature, J. Eur. Ceram. Soc. 31 (2011) 2535–2542, https://doi.org/10.1016/j.jeurceramsoc.2011.01.019.

[25] B. Schamberger, R. Ziege, K. Anselme, M. Ben Amar, M. Bykowski, A.P.G. Castro, A. Cipitria, R.A. Coles, R. Dimova, M. Eder, S. Ehrig, L.M. Escudero, M.E. Evans, P. R. Fernandes, P. Fratzl, L. Geris, N. Gierlinger, E. Hannezo, A. Iglič, J.J. K. Kirkensgaard, P. Kollmannsberger, Ł. Kowalewska, N.A. Kurniawan, I. Papantoniou, L. Pieuchot, T.H.V. Pires, L.D. Renner, A.O. Sageman-Furnas, G. E. Schröder-Turk, A. Sengupta, V.R. Sharma, A. Tagua, C. Tomba, X. Trepat, S. L. Waters, E.F. Yeo, A. Roschger, C.M. Bidan, J.W.C. Dunlop, Curvature in biological systems: its quantification, emergence, and implications across the scales, Adv. Mater. (2023), 2206110, https://doi.org/10.1002/adma.202206110.

[26] M. Paris, A. Götz, I. Hettrich, C.M. Bidan, J.W.C. Dunlop, H. Razi, I. Zizak, D. W. Hutmacher, P. Fratzl, G.N. Duda, W. Wagermaier, A. Cipitria, Scaffold curvature-mediated novel biomineralization process originates a continuous soft tissue-to-bone interface, Acta Biomater. 60 (2017) 64–80, https://doi.org/10.1016/j.actbio.2017.07.029.

[27] S.J.P. Callens, R.J.C. Uyttendaele, L.E. Fratila-Apachitei, A.A. Zadpoor, Substrate curvature as a cue to guide spatiotemporal cell and tissue organization, Biomaterials 232 (2020), 119739, https://doi.org/10.1016/j.biomaterials.2019.119739.

[28] H.A. Almeida, P.J. Bártolo, Tensile and shear stress evaluation of Schwartz surfaces for scaffold design, Procedia Eng. 110 (2015) 167–174, https://doi.org/10.1016/j.proeng.2015.07.025.

[29] L. Lutterotti, S. Matthies, H.R. Wenk, MAUD: A Friendly Java Program for Material Analysis Using Diffraction, 1999.
[30] M. Mathew, L.W. Schroeder, B. Dickens, W.E. Brown, The crystal structure of [alpha]-Ca3(PO4)2, Acta Crystallogr. Sect. B 33 (1977) 1325–1333, https://doi.org/10.1107/S0567740877006037.
[31] M. Yashima, A. Sakai, T. Kamiyama, A. Hoshikawa, Crystal structure analysis of β-tricalcium phosphate Ca 3(PO4)2 by neutron powder diffraction, J. Solid State Chem. 175 (2003) 272–277, https://doi.org/10.1016/S0022-4596(03)00279-2.
[32] S. Graulis, D. Chateigner, R.T. Downs, A.F.T. Yokochi, M. Quirós, L. Lutterotti, E. Manakova, J. Butkus, P. Moeck, A. Le Bail, Crystallography Open Database - an open-access collection of crystal structures, J. Appl. Crystallogr. 42 (2009) 726–729, https://doi.org/10.1107/S0021889809016690.
[33] M. Bohner, B.L.G. Santoni, N. Döbelin, β-tricalcium phosphate for bone substitution: Synthesis and properties, Acta Biomater. 113 (2020) 23–41, https://doi.org/10.1016/j.actbio.2020.06.022.
[34] D. Brazete, P.M.C. Torres, J.C.C. Abrantes, J.M.F. Ferreira, Influence of the Ca/P ratio and cooling rate on the allotropic α↔β-tricalcium phosphate phase transformations, Ceram. Int. 44 (2018) 8249–8256, https://doi.org/10.1016/j.ceramint.2018.02.005.
[35] R.G. Carrodeguas, A.H. De Aza, X. Turrillas, P. Pena, S. De Aza, New approach to the β→α polymorphic transformation in magnesium-substituted tricalcium phosphate and its practical implications, J. Am. Ceram. Soc. 91 (2008) 1281–1286, https://doi.org/10.1111/j.1551-2916.2008.02294.x.
[36] A. Destainville, E. Champion, D. Bernache-Assollant, E. Laborde, Synthesis, characterization and thermal behavior of apatitic tricalcium phosphate, Mater. Chem. Phys. 80 (2003) 269–277, https://doi.org/10.1016/S0254-0584(02)00466-2.
[37] H.-S. Ryu, H.-J. Youn, K.S. Hong, B.-S. Chang, C.-K. Lee, S.-S. Chung, An Improvement in Sintering Property of B-tricalcium Phosphate by Addition of Calcium Pyrophosphate, 2002.
[38] A.C.S. Dantas, W. Acchar, Effect of the mg2+ substitution on the sintering behavior and compressive strength of doped B-TCP/CPP ceramics, Mater. Sci. Forum 798–799 (2014) 466–471, https://doi.org/10.4028/www.scientific.net/MSF.798-799.466.
[39] P. Miranda, E. Saiz, K. Gryn, A.P. Tomsia, Sintering and robocasting of β-tricalcium phosphate scaffolds for orthopaedic applications, Acta Biomater. 2 (2006) 457–466, https://doi.org/10.1016/j.actbio.2006.02.004.
[40] C. Schmidleithner, S. Malferrari, R. Palgrave, D. Bomze, M. Schwentenwein, D. M. Kalaskar, Application of high resolution DLP stereolithography for fabrication of tricalcium phosphate scaffolds for bone regeneration, Biomed. Mater. 14 (2019), https://doi.org/10.1088/1748-605X/ab279d.
[41] B. Waloddi Weibull, A. Statistical Distribution Function of Wide Applicability, n.d.
[42] L.L. Hench, 8 - The skeletal system, in: L.L. Hench, J.R. Jones (Eds.), Biomaterials, Artificial Organs and Tissue Engineering, Woodhead Publishing, 2005, pp. 79–89, https://doi.org/10.1533/9781845690861.2.79.
[43] P. Miranda, A. Pajares, F. Guiberteau, F.L. Cumbrera, B.R. Lawn, Role of flaw statistics in contact fracture of brittle coatings, Acta Mater. 49 (2001) 3719–3726, https://doi.org/10.1016/S1359-6454(01)00280-4.
[44] C. Paredes, F.J. Martínez-Vázquez, A. Pajares, P. Miranda, Co-continuous calcium phosphate/polycaprolactone composite bone scaffolds fabricated by digital light processing and polymer melt suction, Ceram. Int. 47 (2021) 17726–17735, https://doi.org/10.1016/j.ceramint.2021.03.093.
[45] C. Paredes, F.J. Martínez-Vázquez, A. Pajares, P. Miranda, Novel strategy for toughening robocast bioceramic scaffolds using polymeric cores, Ceram. Int. 45 (2019) 19572–19576, https://doi.org/10.1016/j.ceramint.2019.06.175.
[46] J. Bin Lee, W.Y. Maeng, Y.H. Koh, H.E. Kim, Porous calcium phosphate ceramic scaffolds with tailored pore orientations and mechanical properties using lithography-based ceramic 3D printing technique, Materials 11 (2018), https://doi.org/10.3390/ma11091711.
[47] O. Al-Ketan, D.W. Lee, R. Rowshan, R.K. Abu Al-Rub, Functionally graded and multi-morphology sheet TPMS lattices: design, manufacturing, and mechanical properties, J. Mech. Behav. Biomed. Mater. 102 (2020), https://doi.org/10.1016/j.jmbbm.2019.103520.
[48] P. Miranda, A. Pajares, E. Saiz, A.P. Tomsia, F. Guiberteau, Mechanical properties of calcium phosphate scaffolds fabricated by robocasting, J. Biomed. Mater. Res. Part A 85 (2008) 218–227, https://doi.org/10.1002/jbm.a.31587.
[49] F.J. Martínez-Vázquez, F.H. Perera, I. Van Der Meulen, A. Heise, A. Pajares, P. Miranda, Impregnation of β-tricalcium phosphate robocast scaffolds by in situ polymerization, J. Biomed. Mater. Res. Part A 101 (2013) 3086–3096, https://doi.org/10.1002/jbm.a.34609.
[50] F.J. Martínez-Vázquez, F.H. Perera, P. Miranda, A. Pajares, F. Guiberteau, Improving the compressive strength of bioceramic robocast scaffolds by polymer infiltration, Acta Biomater. 6 (2010) 4361–4368, https://doi.org/10.1016/j.actbio.2010.05.024.
[51] J. Roleček, L. Pejchalová, F.J. Martínez-Vázquez, P. Miranda González, D. Salamon, Bioceramic scaffolds fabrication: Indirect 3D printing combined with ice-templating vs. robocasting, J. Eur. Ceram. Soc. 39 (2019) 1595–1602, https://doi.org/10.1016/j.jeurceramsoc.2018.12.006.
[52] T.S. Keller, I I59 pp I 168, 1994.